BG

GSI

GSI-Preprint-96-04
JANUAR 1996

^{6}He AND NEUTRON MOMENTUM DISTRIBUTIONS FROM ^{8}He IN NUCLEAR BREAK-UP REACTIONS AT 240 MeV/u

T. NILSSON, F. HUMBERT, W. SCHWAB, H. SIMON, M. H. SMEDBERG, M. ZINSER;
Th. BLAICH, M.J.G. BORGE, L.V. CHULKOV, Th.W. ELZE, H. EMLING, H. GEISSEL,
K. GRIMM, D. GUILLEMAUD-MUELLER, P.G. HANSEN, R. HOLZMANN, H. IRNICH,
B. JONSON, J.G. KELLER, H. KLINGLER, A.A. KORSHENINNIKOV, J.V. KRATZ,
R. KULESSA, D. LAMBRECHT, Y. LEIFELS, A. MAGEL, M. MOHAR, A.C. MUELLER,
G. MÜNZENBERG, F. NICKEL, G. NYMAN, A RICHTER, K. RIISAGER,
C. SCHEIDENBERGER, G. SCHRIEDER, B.M. SHERRILL, K. STELZER, J. STROTH,
O. TENGBLAD, W. TRAUTMANN, E. WAJDA, M.V. ZHUKOV, E. ZUDE

(accepted for publication in Nucl. Phys. A)

Gesellschaft für Schwerionenforschung mbH
Postfach 110552 · D-64220 Darmstadt · Germany

SW 96 12

^{6}He and neutron momentum distributions from ^{8}He in nuclear break-up reactions at 240 MeV/u

T. Nilsson[1], F. Humbert[2], W. Schwab[3], H. Simon[2], M.H. Smedberg[1], M. Zinser[3], Th. Blaich[4], M.J.G. Borge[5], L.V. Chulkov[6], Th.W. Elze[7], H. Emling[3], H. Geissel[3], K. Grimm[7], D. Guillemaud-Mueller[10], P.G. Hansen[11], R. Holzmann[3], H. Irnich[3], B. Jonson[1], J.G. Keller[8], H. Klingler[7], A.A. Korsheninnikov[9], J.V. Kratz[4], R. Kulessa[12], D. Lambrecht[4], Y. Leifels[8], A. Magel[3], M. Mohar[3], A.C. Mueller[10], G. Münzenberg[3], F. Nickel[3], G. Nyman[1], A. Richter[2], K. Riisager[11], C. Scheidenberger[3], G. Schrieder[2], B.M. Sherrill[13], K. Stelzer[7], J. Stroth[3], O. Tengblad[14], W. Trautmann[3], E. Wajda[12], M.V. Zhukov[1] and E. Zude[3]

January 22, 1996

1. Fysiska Institutionen, Chalmers Tekniska Högskola, S–412 96 Göteborg
2. Institut für Kernphysik, Technische Hochschule, D–64289 Darmstadt
3. Gesellschaft für Schwerionenforschung (GSI), D–64291 Darmstadt
4. Institut für Kernchemie, Johannes-Gutenberg-Universität, D–55099 Mainz
5. Insto. Estructura de la Materia, CSIC, E–28006 Madrid
6. Russian Scientific Center "Kurchatov Institute", Inst. Gen. and Nucl. Phys., Moscow 123182
7. Institut für Kernphysik, Johann-Wolfgang-Goethe-Universität, D–60486 Frankfurt
8. Institut für Experimentalphysik, Ruhr-Universität Bochum, D–44780 Bochum
9. RIKEN, 2-1 Hirosawa, Wako, Saitama 351-01, Japan
10. Institut de Physique Nucléaire, BP 1, F–91406 Orsay Cedex
11. Institut for Fysik og Astronomi, Aarhus Universitet, DK–8000 Aarhus C
12. Instytut Fizyki, Uniwersytet Jagelloński, PL–30-059 Kraków
13. Michigan State University, East Lansing, MI 48824-1321, USA
14. PPE Division, CERN, CH–1211 Genève 23

Abstract

Neutron and ^{6}He momentum distributions from ^{8}He break-up reactions in a C target have been measured at 240 MeV/u. The two-neutron removal cross section was found to be σ_{-2n}=0.27±0.03 b. The nature of the momentum distributions is interpreted in some simple reaction scenarios.

Keywords: secondary radioactive beams, exotic nuclei, halo nuclei, ^{8}He, momentum distribution, invariant mass spectra, fragmentation mechanism, break-up reactions, two neutron removal cross section

1 Introduction

New experimental techniques for producing radioactive beams [1, 2] allow the study of a host of interesting new phenomena in the regions of the neutron and proton drip-lines. One of the most striking examples is the neutron halo of ^{11}Li [3, 4, 5] which can be viewed as made up of two loosely bound neutrons at a large distance surrounding an inert core of ^{9}Li. However, ^{11}Li is not the only nucleus in this region of the nuclear chart showing interesting properties. The case of ^{8}He is also highly interesting, being the nucleus with the highest A/Z-ratio among the known nuclei still stable against particle emission. It is, at present, the closest we can get to "neutron matter" in the laboratory. The first evidence for an anomalous matter distribution in the neutron-rich helium isotopes ^{6}He and ^{8}He was found in the same experiment that gave the first indication of a neutron halo in ^{11}Li [3]. A pronounced increase in the total interaction cross section was seen when going from ^{4}He to ^{6}He and further on to ^{8}He, although this was not as dramatic as in the case of ^{11}Li. The total interaction cross sections, together with the 2n- and 4n-removal cross sections, indicate that the realistic picture of ^{8}He is that of an α-particle core surrounded by four loosely bound neutrons rather than a ^{6}He core surrounded by two halo neutrons [6]. Decay studies made at ISOLDE [7, 8] show a very large branching ratio for beta-delayed triton emission. The large overlap between the wave function of the 9.3 MeV resonance of ^{8}Li (decaying into ^{5}He + t) and the ground state of ^{8}He characterised by reduced Gamow-Teller transition probability (B_{GT} = 5.18) amounting to almost half of the sum-rule value suggests a picture of sizable correlations between the four outer neutrons in ^{8}He. Previously, the extended neutron distribution has mainly been probed in dissociation experiments [9] at 790 MeV/u. In this paper we present results from, and an interpretation of, reaction experiments involving the break-up of ^{8}He projectiles into ^{6}He+n+X at 240 MeV/u.

2 Experiment

The present experiment was performed at the GSI in Darmstadt, where a secondary beam of ^{8}He (240 MeV/u) was produced in a 8 g/cm^{2} beryllium production target from a primary beam of ^{18}O with an energy of 340 MeV/u. The produced nuclei were subsequently

separated using the fragment separator FRS [10]. The ^{8}He could be obtained together with ^{11}Li and ^{14}Be beams by operating the FRS without a degrader, thus separated by pure Bρ-selection. After separation, the beam was transported to the experimental set-up. In order to reach the main experimental area, the beam transport included one turn through the Experimental Storage Ring (ESR). The energies of the secondary beams were thus limited by the maximum rigidity (9.5 Tm) in the ESR.

The dissociation reactions were studied with the set-up shown in figure 1. Directly in front of the reaction target, a thin plastic scintillator detector (POS2), and a position-sensitive multi-wire drift chamber (MWDC-1) were situated. These detectors served to determine the position of the incident beam on the target. Furthermore, the position-sensitive scintillator detector was used to give the time reference for the events. The momentum distributions were measured with a C target of 1.29 g/cm^2 thickness. Data were also taken with a Pb target of 0.30 g/cm^2 thickness but the statistics were insufficient to allow an analysis of the momentum distributions. The target thicknesses were chosen in order to match the angular straggling in the targets to the detector resolution. Behind the secondary target, the charged fragments were deflected in the dipole magnet ALADIN [11] and analysed according to position and bending angle in MWDC-2 and MWDC-3. These chambers had an active area of 70 x 50 cm^2. The charge and velocity of the fragments were determined by measuring the energy loss and time-of-flight (TOF) in a plastic wall, consisting of seven scintillator paddles.

The neutrons were detected in the Large Area Neutron Detector (LAND) [12], which was positioned 11 m from the target. The LAND detector consists of 200 modules, paddles, each made up of alternating layers of iron and plastic scintillator. The scintillators detect hadronic showers created by highly energetic neutrons in the iron converter material. The active volume of each module is 0.1 x 0.1 x 2 m^3 and they are alternately aligned along the vertical and horizontal directions, forming layers of 2 x 2 m^2 with 0.1 m thickness. The total active volume of the detector is 2 x 2 x 1 m^3. The position resolution in the direction perpendicular to the paddle is given by the granularity, i.e. the paddle width. In the direction along the paddle, the position resolution is determined by a number of factors, such as time resolution and the size of the hadronic shower created. This has been experimentally determined to be 5.1 cm [12] for a single neutron of energy 240 MeV. The LAND detector has an intrinsic efficiency of 85$\pm$6 % for detecting single neutrons with an energy of 240 MeV [13].

All multi-wire drift chambers were of identical design as illustrated in figure 2. Each wire-plane consisted of alternating anode and cathode wires with a spacing of 5 mm. This constituted the maximum drift distance. The anode wires were 20 μm in diameter and the cathode wires 50 μm. The latter were mounted in pairs with an internal distance of 500 μm in order to increase the charge collection [14]. The anode wires were bussed together via a delay-line which was read out at both ends. Thus, by comparing the time of arrival for the pulse to the left and right end of the delay line, the wire which had fired could be deduced according to

$$t_L - t_R = (2n - N)t_{delay}, \tag{1}$$

(see also figure 2, where n and N are defined). The sum of the two times read out only

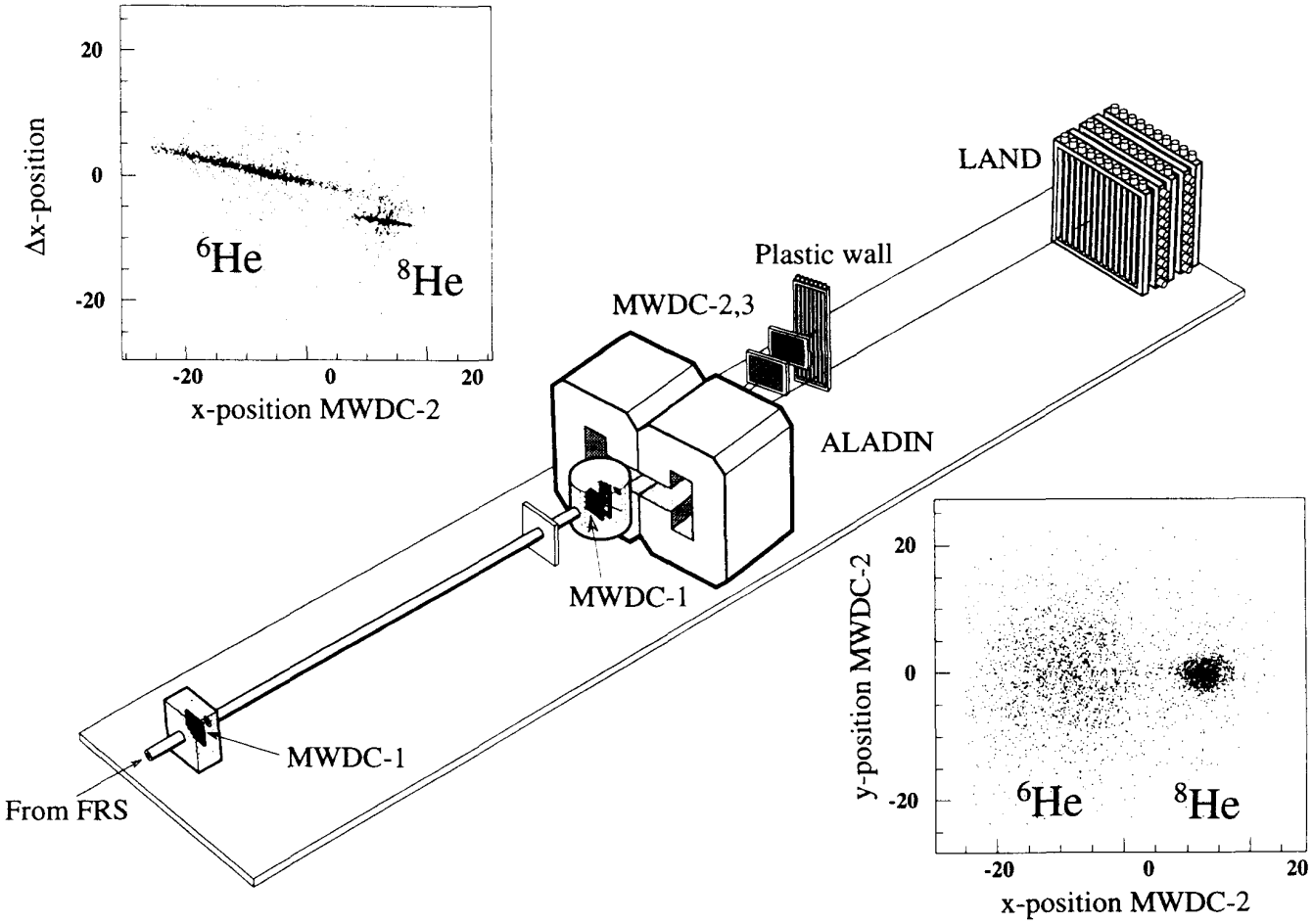

Figure 1: The experimental set-up. The incoming beam was defined by a MWPC at the entrance of the cave and a MWDC (MWDC-1) situated close to the secondary target. The charged fragments were deflected and analysed in the dipole magnet ALADIN in conjunction with MWDC-2 and -3. Behind the second drift chamber, a plastic wall was situated, yielding TOF and Z information. The neutrons were detected in the large area neutron detector LAND. The lower right inset shows the positions of ^{8}He and ^{6}He in MWDC-2. In the upper left scatterplot, the difference between the x-positions in MWDC-2 and MWDC-3, approximately corresponding to the bending angle in ALADIN, is plotted as a function of the x-position in MWDC-2. As can be seen, a reliable separation of the different isotopes could be made.

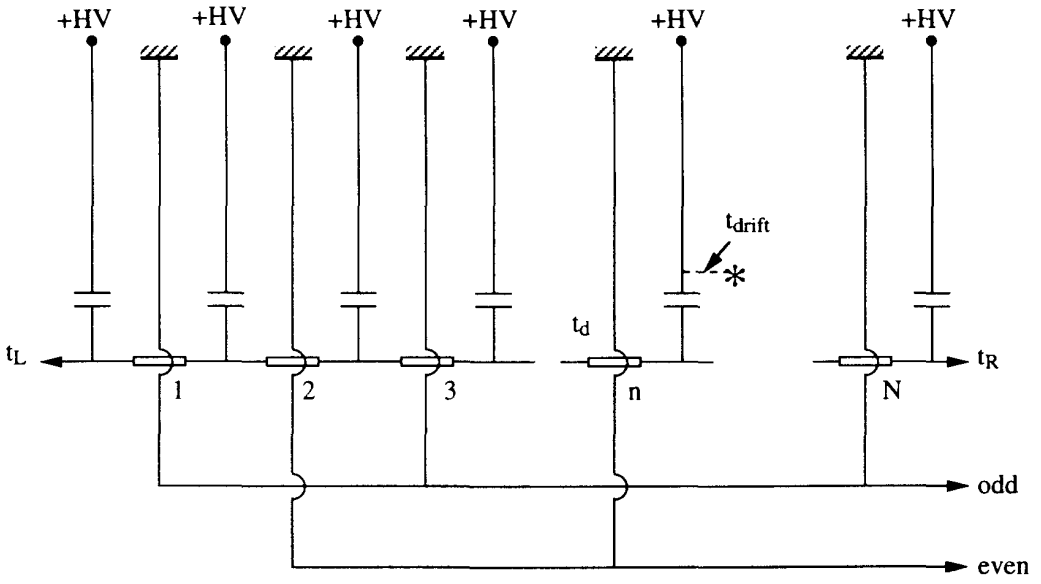

Figure 2: Schematic picture of the MWDC read-out. The anode wires are all connected to a delay line with a fixed delay between the wirespaces which is read out at both ends, yielding the LEFT and RIGHT signal according to $t_L = t_{drift} + nt_{delay}$ and $t_R = t_{drift} + (N-n)t_{delay}$. A read-out of the cathode wires with even or odd numbers indicates whether the ion track is to the right or the left of the anode wire.

depends upon the drift time, since the delay-line then simply gives a constant contribution.

$$t_L + t_R = 2t_{drift} + Nt_{delay} \tag{2}$$

The only remaining ambiguity was whether the ion passed to the left or to the right of the anode wire. This could be solved by using the signals induced in the cathode wires, as these are sensitive to which side of the anode wire the secondary avalanche takes place. The cathode wires were alternately connected to two signal lines, and by comparing the odd and even signals, a position assignment could be made. An additional consistency check was provided by recording the time of one of the cathode signals. It is defined by the secondary ionisation in the close vicinity of the anode wire and can thus be expressed as

$$t_C \approx t_{drift}. \tag{3}$$

This made it possible to calculate a *checksum* variable according to

$$t_{check} = t_L + t_R - 2t_C \approx Nt_{delay}. \tag{4}$$

As can be seen from equations (2) and (3), this entity should be practically constant for a correct event. A multiple hit could give an alleged erroneous position if the pulses recorded left and right do not stem from the same ion. By applying a cut in the checksum variable, these events could be discarded. Although the MWDCs showed a non-linear dependence between drift time and ion position, it was possible to obtain a position resolution of 2 mm with high efficiency [15].

The set-up was optimised for the reaction channel ^{11}Li $\rightarrow$ ^{9}Li + n + n [16]. As a consequence, the acceptance was limited with respect to other reactions, as can be seen in

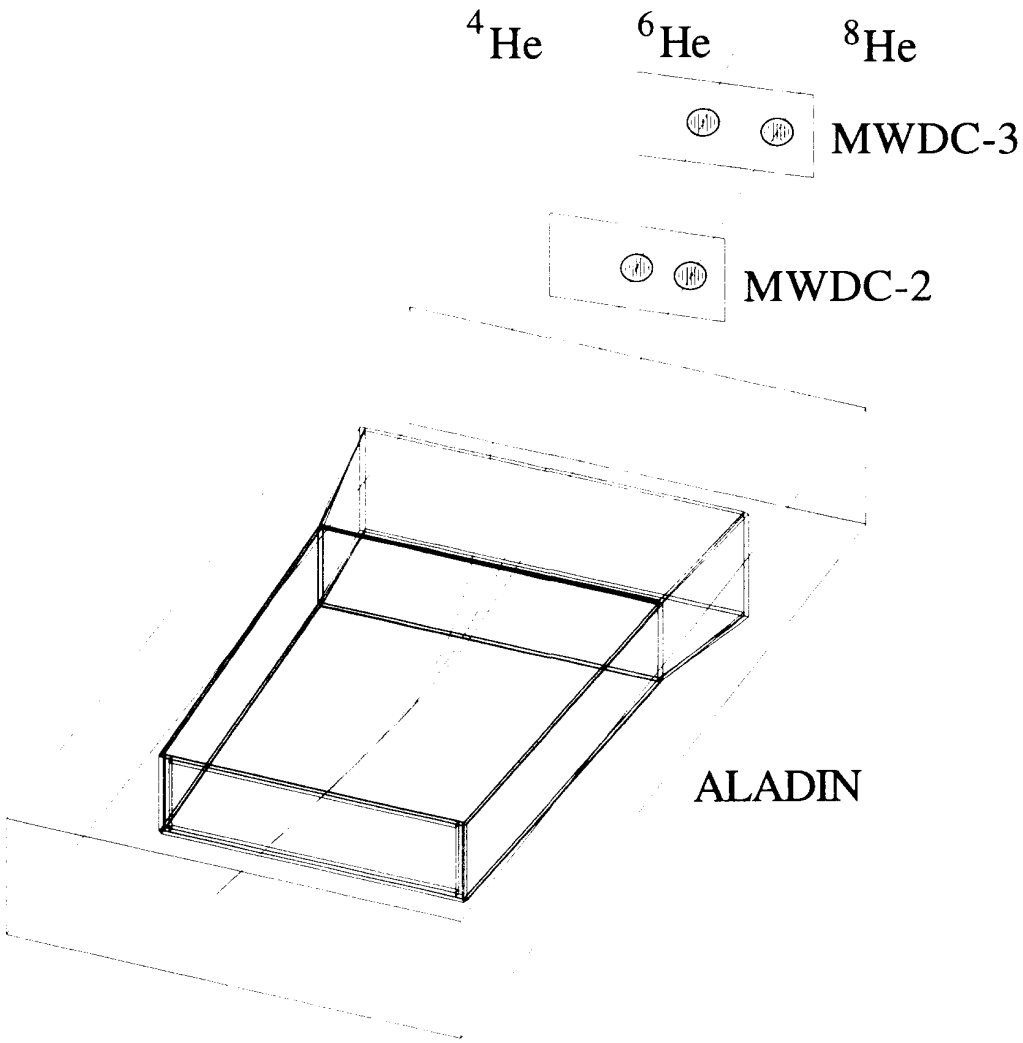

Figure 3: Ion tracking for ^{8}He, ^{6}He and ^{4}He. The ^{4}He ions are bent strongly and therefore not recorded.

figure 3. The very fundamental reaction channel $^{8}\text{He} \rightarrow {}^{4}\text{He} + \text{X}$ was therefore excluded by the restricted acceptance in this experiment.

3 Theory

The momentum distributions of particles detected in a fragmentation experiment are determined not only by their internal motion in the projectile, i.e. by a projectile wave function, but also by the fragmentation mechanism. Projectile fragmentation of ^{8}He, as well as ^{6}He and ^{11}Li, has earlier been measured at the energy 790 MeV/u [9]. The momentum widths of the particles were later interpreted in a semiquantitative analysis [17], where it was found that that the result could be accounted for as a sequential decay via intermediate resonances, such as ^{5,7}He and ^{10}Li, as the dominant reaction mechanism for the two-neutron removal process. The consequences of such intermediate resonances have

also been thoroughly investigated in ref. [18, 19]. In ref. [20] detailed calculations for the α-particle and neutron momentum distributions from the fragmentation of ^{6}He on a carbon target at high energy were carried out. The nucleus ^{6}He was chosen since its wave function is well established [21] and thus an excellent tool to investigate the fragmentation mechanism. In order to describe the experimental data, one had to consider the n-target nucleus scattering in the Glauber approach and the n+^{4}He final state interaction at the resonance ^{5}He. In this case, the α-particle momentum distribution from ^{6}He fragmentation is close to the α-particle distribution in ^{6}He. However, to describe the neutron momentum distribution, the inclusion of both ingredients, n-target nucleus scattering and intermediate ^{5}He resonance, was essential. Recently, it was demonstrated [22] that the experimental data for the break-up of ^{8}He into ^{6}He and two neutrons at 790 MeV/u can be reproduced well - assuming the same reaction mechanism (n-target nucleus scattering and n-^{6}He final state interaction through the ^{7}He resonance), and using a COSMA (Cluster Orbital Shell Model Approximation) wave function for the ^{8}He nucleus.

The COSMA wave function for ^{8}He was obtained in a five body (α+4n) approach, where each valence neutron occupies a $0p_{3/2}$ state relative to the α core. For the radial n-α motion, oscillator wave functions were used. The Pauli principle, which was taken into account strictly, is responsible for exotic correlations of the valence neutrons as discussed in ref. [23]. As a result, the ^{8}He wave function can be written as a Slater determinant constructed with the help of four single-particle wave functions $\psi_i(\mathbf{r}_k, \sigma_k)$, $i,k = 1,\ldots,4$, corresponding to different projections of the j=3/2 angular momentum:

$$\psi_i(\mathbf{r}_k, \sigma_k) = \varphi(r_k) \cdot \sum_{m_i \nu_i} \Big\langle 1 m_i \frac{1}{2} \nu_i \Big| \frac{3}{2} (\frac{3}{2} + 1 - i) \Big\rangle Y_{1m_i}(\mathbf{r}_k/r_k) \chi_{\nu_i}(\sigma_k) \ , \tag{5}$$

$$\varphi(r) = \sqrt{\frac{8}{3\sqrt{\pi}\, r_0^3}} \ (\frac{r}{r_0}) \ \exp(\frac{-r^2}{2r_0^2}). \tag{6}$$

Here, χ_{ν_i}, $\nu_i = \pm 1/2$ is the spin wave function, and $\varphi(r)$ the standard $0p$ radial oscillator wave function. The coordinates $\mathbf{r}_i$ are measured from the center of mass of the α core to the valence neutrons. The wave function in equation (6) contains only one free parameter, the oscillator length r_0. This parameter was adjusted [23] to reproduce the experimental r.m.s. radius of ^{8}He, according to

$$8R^2(^8He) - 4R^2(^4He) = \frac{35}{4} r_0^2. \tag{7}$$

With the values 1.45 fm [21] and 2.52 fm [24] for the matter r.m.s radii, R, of the α particle and ^{8}He respectively, the corresponding value for the oscillator length is r_0=2.20 fm.

In the simplest model, which is known as the Serber model or the sudden approximation, the momentum distribution of a high energy projectile fragment is determined by its internal motion in the projectile only. Thus, to calculate the particle momentum distributions in ^{8}He, we need to transform the wave function to the momentum representation, square it and sum over the spin variables. For the neutron momentum distribution, we get the expression

$$\rho_n(\mathbf{p}_n) = \frac{2}{3\pi^{3/2} p_0^5} \mathbf{p}_n^2 \exp\Big(-\frac{\mathbf{p}_n^2}{p_0^2}\Big), \tag{8}$$

where $\mathbf{p}_n$ is the c.m. momentum of the neutron and $p_0 = \hbar/r_0$. Finally, this three-dimensional distribution has to be integrated over momenta in order to reproduce the experimental conditions. This gives rise to a neutron momentum distribution which is far too wide as compared to the experimental data (see for example the dotted curve in figure 7). As in [20, 22], we therefore assume that the dominant reaction mechanism for ^{8}He fragmentation on a light target is connected with the one-neutron removal process, illustrated in figure 4. This picture is supported by the average neutron multiplicity measured to be close to one for the C target (see section 4.1), as the removed neutron is scattered to large angles not covered by our detector. Furthermore the assumption is justified by the invariant mass spectrum shown in section 4.2, since after one neutron has been removed, we have the ^{7}He subsystem (n+^{6}He) with quantum numbers $J^\pi = (3/2)^-$. This ^{7}He resonance are clearly seen in figure 5. The ^{7}He motion is assumed to be given by the motion of the removed neutron in ^{8}He. The residual n+^{6}He subsystem is influenced by final-state interactions at the ^{7}He resonance. To describe the ^{7}He decay, we use the Breit-Wigner formula,

$$I_{B-W}(E) = \frac{\Gamma}{2\pi} \frac{1}{(E - E_0)^2 + \frac{\Gamma^2}{4}}, \tag{9}$$

with parameters E_0 and Γ. The Γ parameter is taken as a constant since its energy dependence can be neglected when considering the single neutron momentum distribution. The observed ^{6}He transverse momentum distribution then has the form

$$\frac{dN_{^6He}}{dp_y} = \int \rho_n(\frac{7}{6}\mathbf{p}') I_{B-W}(\mathbf{p}'') \delta(\mathbf{p}' + \mathbf{p}'' - \mathbf{p}) d\mathbf{p}' d\mathbf{p}'' dp_x dp_z, \tag{10}$$

since $(\frac{7}{6}\mathbf{p}')$ is the ^{7}He momenta in the ^{8}He c.m., expressed in ^{6}He momenta $\mathbf{p}'$, and

$$\frac{7}{6}\mathbf{p}' = -\mathbf{p}_{removed}, \tag{11}$$

where $\mathbf{p}_{removed}$ is the momenta of the removed neutron scattered on the target nucleus. Similarly, we have for the radial neutron momentum distribution

$$\frac{dN_n^{FSI}}{p_r dp_r} = 2\pi \int \rho_n(7\mathbf{p}''') I_{B-W}(\mathbf{p}'') \delta(\mathbf{p}''' + \mathbf{p}'' - \mathbf{p}) d\mathbf{p}''' d\mathbf{p}'' dp_z, \tag{12}$$

where

$$7\mathbf{p}''' = -\mathbf{p}_{removed}. \tag{13}$$

In equation (10) and (12) $\mathbf{p}''$ is the momentum of the ^{6}He or the neutron in the ^{7}He c.m., connected with E from equation (9) by

$$E = \frac{\mathbf{p}''^2}{2(\frac{6m}{7})}, \tag{14}$$

where m is the nucleon mass. Since ^{6}He is heavy, the momentum distribution for ^{6}He is not very sensitive to the position of the ^{7}He resonance, i.e. E_0. However this is not the case for the neutron, due to its lower mass. Therefore the knowledge of the exact energy of the ^{7}He resonance is important in calculations of the neutron momentum width.

The momentum distribution of the neutron scattered on the carbon target was calculated in a Glauber approach, and gives rise to a broad component in the spectrum. The resulting

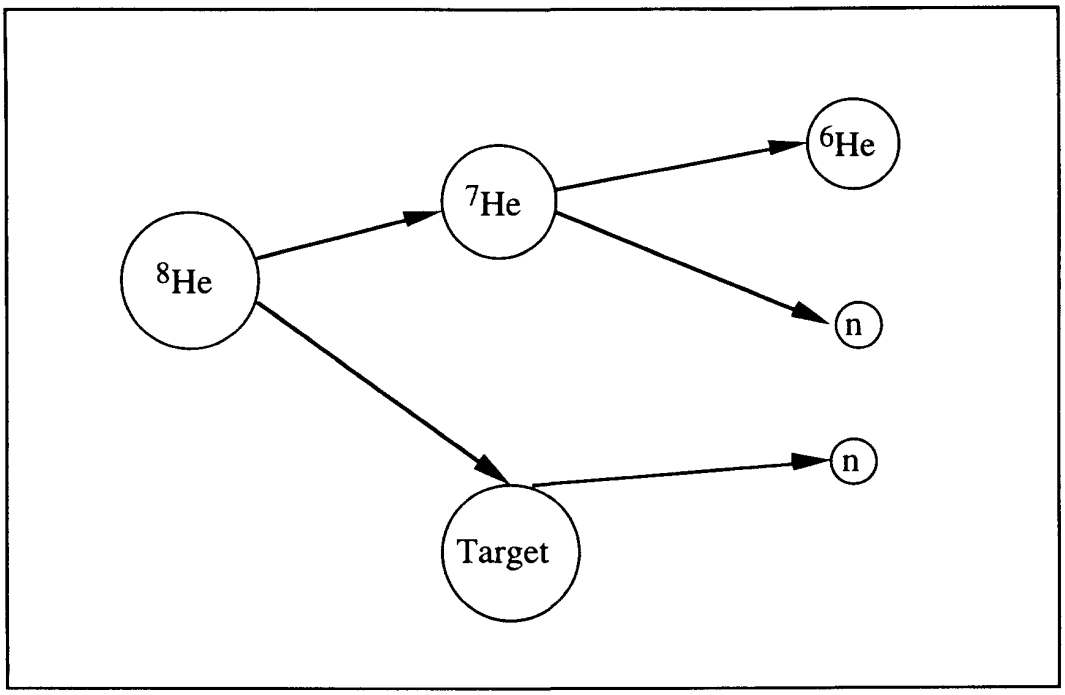

Figure 4: Schematic picture of the dominated fragmentation mechanism in the ^{8}He $\rightarrow$ ^{6}He disintegration channel at 240 MeV/u.

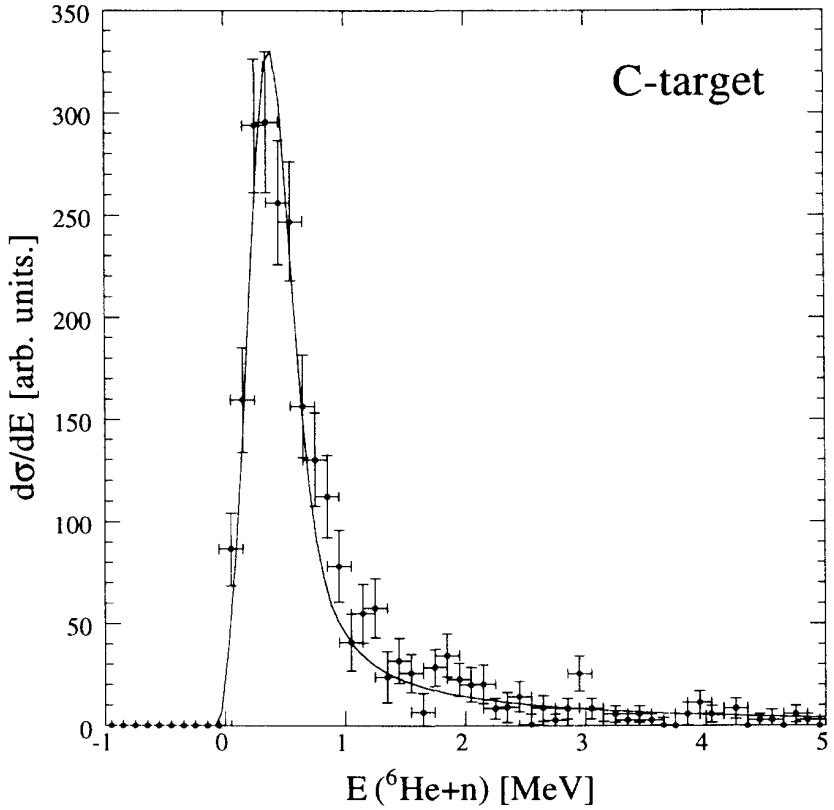

Figure 5: Relative energy distribution of the ^{6}He+n system from dissociation of ^{8}He at 240 MeV/u

neutron radial momentum distribution is then a product of the Glauber term [22] and the initial motion (equation (8)) in ^{8}He, and has the form

$$\frac{dN_n^{Glauber}}{p_r dp_r} = 2\pi \int \rho_n(\mathbf{p}') \mid F_{Glauber}(\mathbf{q}) \mid^2 \delta(\mathbf{p}' + \mathbf{q} - \mathbf{p}) d\mathbf{p}' d\mathbf{q} dp_z, \tag{15}$$

where $\mathbf{q}$ is the 2-dimensional momentum transfer vector, perpendicular to the beam axis. The observed neutron momentum distribution is then the sum of equations (12) and (15) with equal weight.

4 Results

4.1 Cross section and neutron multiplicity

When plotting the difference of the x-position in MWDC-2 and in MWDC-3, approximately corresponding to the bending angle in ALADIN, as a function of the x-position in MWDC-2, a reliable isotope identification could be obtained. (See the inset of figure 1.) From the ratio of ^{8}He ions breaking up into ^{6}He with and without target, the two-neutron removal cross section could be deduced as σ_{-2n}=0.27±0.03 b. The apparent neutron multiplicity accompanying the ^{8}He → ^{6}He disintegration channel could be determined. Within the acceptance of LAND ($p_r \leq$ 60 MeV/c) we observe zero, one and two neutrons in coincidence with ^{6}He fragment with relative intensities of 20±3, 71±9 and 9±2 per cent respectively. Thus the average neutron multiplicity is close to one as already mentioned in section 3 when discussing the reaction mechanisms involved.

4.2 The ^{6}He+n resonance

The invariant mass spectrum of the intermediate resonance, ^{7}He, is shown in figure 5. It is presented as a function of the relative energy, E(^{6}He+n), in the ^{6}He+n system defined by

$$E(^6He + n) = \sqrt{(E_{^6He} + E_n)^2 - (\mathbf{p}_{^6He} + \mathbf{p}_n)^2 c^2} - M_{^6He}c^2 - M_n c^2, \tag{16}$$

where $E_{^6He}$ (E_n) and $\mathbf{p}_{^6He}$ ($\mathbf{p}_n$) are total energy and momentum for the fragment (neutron). This Lorentz-invariant quantity is the excitation energy measured from the ^{6}He+n threshold. We note from the figure that the entire distribution is described well by a single resonance state. When corrected for the instrumental resolution, better than 500 keV FWHM in the relevant range of energy, the resonance energy, E_0, is found to be 0.38±0.02±0.08 MeV (where the latter term represents the uncertainty in the energy calibration) above the ^{6}He+n threshold with a width Γ of 0.18±0.02 MeV. We identify this resonance as the ^{7}He ground state for which E_0=0.44±0.03 MeV and Γ=0.16±0.03 MeV has been reported earlier [25]. Thus, the observed width in our experiment is in perfect agreement, while for the resonance energy a small difference is found, still within our experimental uncertainty. The value of E_0=0.44 MeV is used in the subsequent calculations if not otherwise stated. From the invariant mass spectrum in figure 5 together with the

neutron multiplicity, we conclude that also at the energy 240 MeV/u the dominant mechanism is sequential, where one neutron is removed from ^{8}He, leaving ^{7}He in its ground state which in turn disintegrates by neutron emission.

4.3 Momentum distributions

The momentum distributions were extracted in different ways for the charged fragments and the neutrons. In the case of the neutrons, the detected position of the impinging neutron was converted into a radial momentum. As the LAND detector has a rather good position resolution (better than 7 MeV/c when expressed as transverse momentum) in the plane perpendicular to the beam axis, only an integration along this axis (z-axis) was made. We call this the radial momentum distribution W_2 (for axial symmetry), which can be obtained as an integral of the three-dimensional momentum distribution

$$W_3 = \frac{d^3N}{dp_x dp_y dp_z} \tag{17}$$

$$W_2 = \frac{d^2N}{dp_x dp_y} = \frac{dN}{2\pi p_r dp_r} = \int W_3 dp_z, \quad p_r = \sqrt{p_x^2 + p_y^2} \tag{18}$$

It was also possible to perform a two-fold integration along the beam axis and one of the axes perpendicular to the beam, according to

$$W_1 = \frac{dN}{dp_y} = \int W_3 dp_x dp_z. \tag{19}$$

The neutron distribution was fitted with Gaussian and Lorentzian distribution functions. The shape of the experimentally determined distribution was satisfactorily described by a single Gaussian, whereas the simple Lorentzian could not properly describe the data. For the doubly integrated momentum distribution, W_1, the Gaussian fit yields the same width as for the W_2-distribution. This is another indication, as shown in [26], for a momentum distribution that factorizes (as do the Gaussian) since the lineshape then is unchanged by an integration. In the case of the charged fragments, the y-position in the MWDC-2 (the direction perpendicular to the ALADIN bending plane) was used. Here, the position is not perturbed by the bending, and corresponds directly to the transverse momentum. Here also, the best fit was obtained by a single Gaussian. A deconvolution of the true momentum width and the beam spread, deduced from the non-reacting ^{8}He (Γ_{eff} = 31 MeV/c), could thus easily be made. The momentum distributions shown in this work all stem from the reaction ^{8}He $\rightarrow$ ^{6}He + n + X. This means no limitation as the ^{6}He momentum distribution from the reaction ^{8}He $\rightarrow$ ^{6}He + X has identical shape. The neutron and ^{6}He widths for reactions with the carbon target are given in table 1. As previously mentioned, the counting statistics were insufficient to extract reliable momentum distributions for the reactions in lead target.

The ^{6}He and the neutron momentum distributions measured at 240 MeV/u are found to be narrower than the distributions at the energy 790 MeV/u. As already mentioned, the high energy data have successfully been reproduced [22] with a COSMA wave function for ^{8}He together with the reaction mechanism described in section 3. When repeating the

Table 1: Widths of the single radial neutron and transverse fragment distributions from break-up in a carbon target using Gaussian fits. The values in the brackets are the corresponding transverse widths for the neutrons.

	σ_{Gauss} (MeV/c)	Γ_{eff} [a] (MeV/c)
n	20.5(21.2) ± 1.5	48.2(49.8) ± 3.5
^{6}He	56 ± 3	132 ± 7

a) To help the comparison with data analysed in terms of Lorentzian momentum distributions, we give here an effective width $\Gamma_{eff} = 2.35\ \sigma$

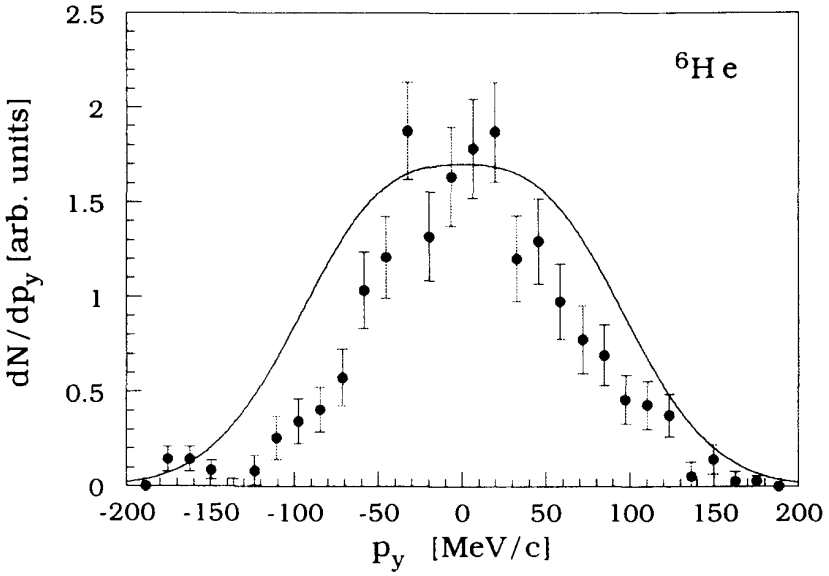

Figure 6: Transverse momentum distribution of ^{6}He from a carbon target at the energy 240 MeV/u. The curve was calculated with a COSMA wave function for ^{8}He together with the reaction mechanism in figure 4.

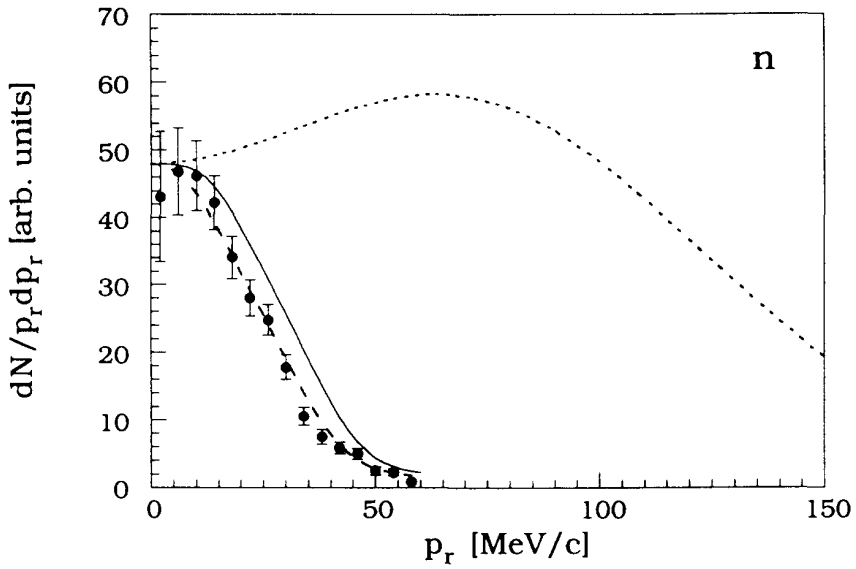

Figure 7: Radial momentum distribution of neutrons detected in coincidence with ^{6}He from reaction of ^{8}He with a carbon target at the energy 240 MeV/u. The curves were calculated with a COSMA wave function for ^{8}He together with the reaction mechanism in figure 4. The fully drawn and the dashed curves correspond to the resonance energies E_0=0.44 MeV and 0.32 MeV respectively. For comparison we also show, as a dotted curve, the very broad momentum distribution obtained in the sudden approximation, i.e. equation (8) integrated over longitudinal momenta p_z. This broad distribution just corresponds to the neutron momentum distribution inside ^{8}He.

calculation for the neutron momentum distribution for the lower energy, we find that there is no significant dependence of beam energy in this reaction scenario. In fact, the only difference arises in the Glauber term in equation (15) which contains the energy dependent elementary nucleon-nucleon cross section. But, since the distribution $dN_n^{Glauber}/p_r dp_r$ in any case is much broader than $dN_n^{FSI}/p_r dp_r$, the difference in neutron momentum widths at the two different beam energies will be completely negligible (Note that we have used a relative weight for the distributions (12) and (15), which corresponds to equal norms obtained by integration of these distributions over full momentum ranges.). This means that the calculation overestimates both neutron and ^{6}He momentum widths for projectiles of energy 240 MeV/u. This can easily be seen in figure 6, where we show the measured ^{6}He transverse momentum distribution compared with the calculated result of equation (10) which describes the high energy data rather well [23]. We would also like to mention that our calculated curve is close to the broad ^{6}He transverse momentum distribution obtained in a stochastical variational approach [27]. In figure 7 we show the experimental radial neutron momentum measured in coincidence with ^{6}He. The calculated curves correspond to the sum of equations (12) and (15) with equal weights. In the full drawn curve, we have used the Breit-Wigner formula (9) with the parameters E_0=0.44 MeV and Γ=0.16 MeV. Note that with this choice of parameters it was possible to reproduce the experimental neutron momentum width at 790 MeV/u [22]. In order to demonstrate the large sensitivity of the neutron width to the position of the ^{7}He resonance, we show as an example a calculation where we used the value E_0=0.32 MeV and Γ=0.16 MeV as a dashed curve.

4.4 Beam energy dependence of the momentum widths

In figure 8, we give the measured momentum widths of the neutrons and ^{6}He fragments from ^{8}He break-up at different beam energies. It is noteworthy that the preliminary result for the ^{6}He momentum distribution at the energy 55 MeV/u [28] shows an even narrower width than found at 240 MeV/u. A similar tendency of increasing momentum width with beam energy has been found earlier in the break-up of ^{11}Li; see, for example, figure 1 in ref. [30] where the momentum widths at different beam energies are summarised. The results shown in figure 8 indicate that the one-neutron removal process via the resonance state of ^{7}He is not the only contributing mechanism to the particle momentum distributions. Therefore, we expect an additional mechanism at lower energy. This process will compete with the one neutron removal process described in section 3, but the latter will gradually begin to dominate as the energy increases. In ref. [31], such an additional mechanism was proposed in order to investigate the consequences of low-lying resonances in the halo nuclei ^{6}He and ^{11}Li. The authors showed that the narrow part of the particle momentum distributions at low beam energy could originate from a sequential decay via a low-lying projectile resonance. We will adopt this idea for the case of ^{8}He, whose excited state (E=3.57±0.12 MeV, Γ=0.5±0.35 MeV) was recently measured [32]. Thus, assume that the ^{8}He projectile is excited, for a light target as carbon by nuclear forces, to its first excited state. This ^{8}He* state lies above the ^{6}He+2n threshold. Neglecting the internal structure of the decaying ^{8}He* state, it will disintegrate into a ^{6}He fragment and two neutrons[1] according to the three-body phase volume (see figure 9). A support for this decay channel, although weak, have been seen in ^{6}He+n+n coincidences. In figure 10 we show the ^{8}He excitation energy spectrum deduced from the invariant mass of the ^{6}He+n+n channel. The full drawn curve reflects the sum of Lorentzian and a smooth background term from the three-body phase space, folded with the experimental response with a resolution of about 1.4 MeV FWHM around the resonance energy. We found that the peak corresponds to a resonance energy, E=3.72±0.24 MeV, and width, Γ=0.53±0.43 MeV, which agree well with the values quoted in ref. [32].

We have calculated the particle momentum distributions when an admixture of this decay channel is added to the one neutron removal channel. In order to reproduce the experimental momentum distribution for the ^{6}He fragment we find that an admixture of about 30% of this reaction channel is needed (see the upper inset in figure 9). However, both the low intensity of the ^{6}He+n+n resonance and the neutron multiplicity indicates that this decay channel is weak as compared to the one neutron removal process. The narrow ^{6}He momentum distribution can therefore not be explained from this channel only, since as shown in figure 9, about 30% is needed to explain the experimental data. Problems are also encountered when calculating the corresponding neutron momentum width, see the lower inset in figure 9. The sequential decay via a ^{8}He resonance gives a characteristic radial width of about 68 MeV/c, as compared with 62 MeV/c (the fully drawn curve in figure 7) for the one neutron removal process, and does not explain the narrow (48.2 MeV/c) experimental momentum distribution. We have also investigated the sequential decay via the ^{7}He resonance, i.e route b.) in figure 9. We found also here that an admixture of about 30% for this decay channel describe the experimental data for the ^{6}He fragment

[1]The $^8He^* \rightarrow {}^4He + 4n$ channel is also open, but was shown [32] to be much weaker, namely with branching ratio $b_{^4He+4n}/b_{^6He+2n} \leq 0.05$

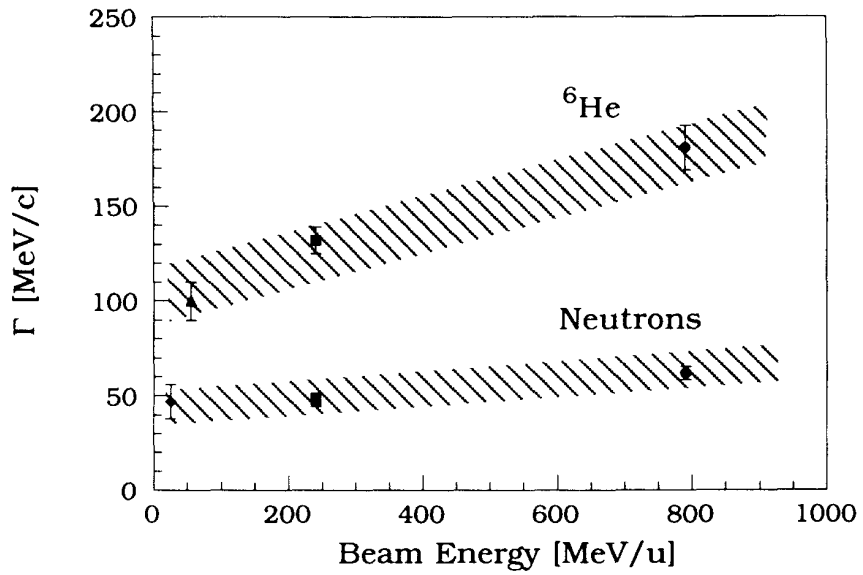

Figure 8: The Full Width Half Maximum, Γ, derived from experimental ^{6}He and neutron distributions after the break up of ^{8}He on light targets (Be, C), as a function of the incident beam energy. The data points are taken from [9] (circle), [28] (triangle),[29] (diamond) and this work (square).

but still overestimates the neutron width. However, before any definite conclusions about a contribution from a reaction mechanism through the ^{8}He excited state can be drawn, it should be kept in mind that the structure of the ^{8}He* state has to be investigated. Furthermore, a possible interference effect between the two competing mechanisms might be considered.

5 Summary

The two-neutron removal cross section for ^{8}He projectiles on a carbon target at the energy 240 MeV/u have been measured. Furthermore, the neutron, in coincidence with ^{6}He, and the ^{6}He momentum distributions from fragmentation of ^{8}He on a carbon target have also been measured. The transverse momentum distribution for the ^{6}He fragment as well as the radial neutron momentum distribution are well described by a single Gaussian curve and have widths (Γ_{eff}) of 132 ± 7 MeV/c and 48.2 ± 3.5 MeV/c respectively. Both these distributions are narrower than the corresponding distributions from break-up of ^{8}He on a carbon target at 790 MeV/u [9]. These results, together with the preliminary result for the ^{6}He width at 55 MeV/u [28], allow us to speculate about the energy dependence of the ^{6}He and neutron momentum widths from ^{8}He fragmentation on a light target. It should be noted that a similar energy dependence of the widths of the core and neutron momentum distributions has been found for the well known neutron halo nucleus ^{11}Li. To fit our data, we use a fragmentation mechanism [20, 22], which describes the high-energy data from ^{6,8}He fragmentation well. However, this reaction mechanism appears to be insufficient to describe the more narrow momentum distributions obtained in this work.

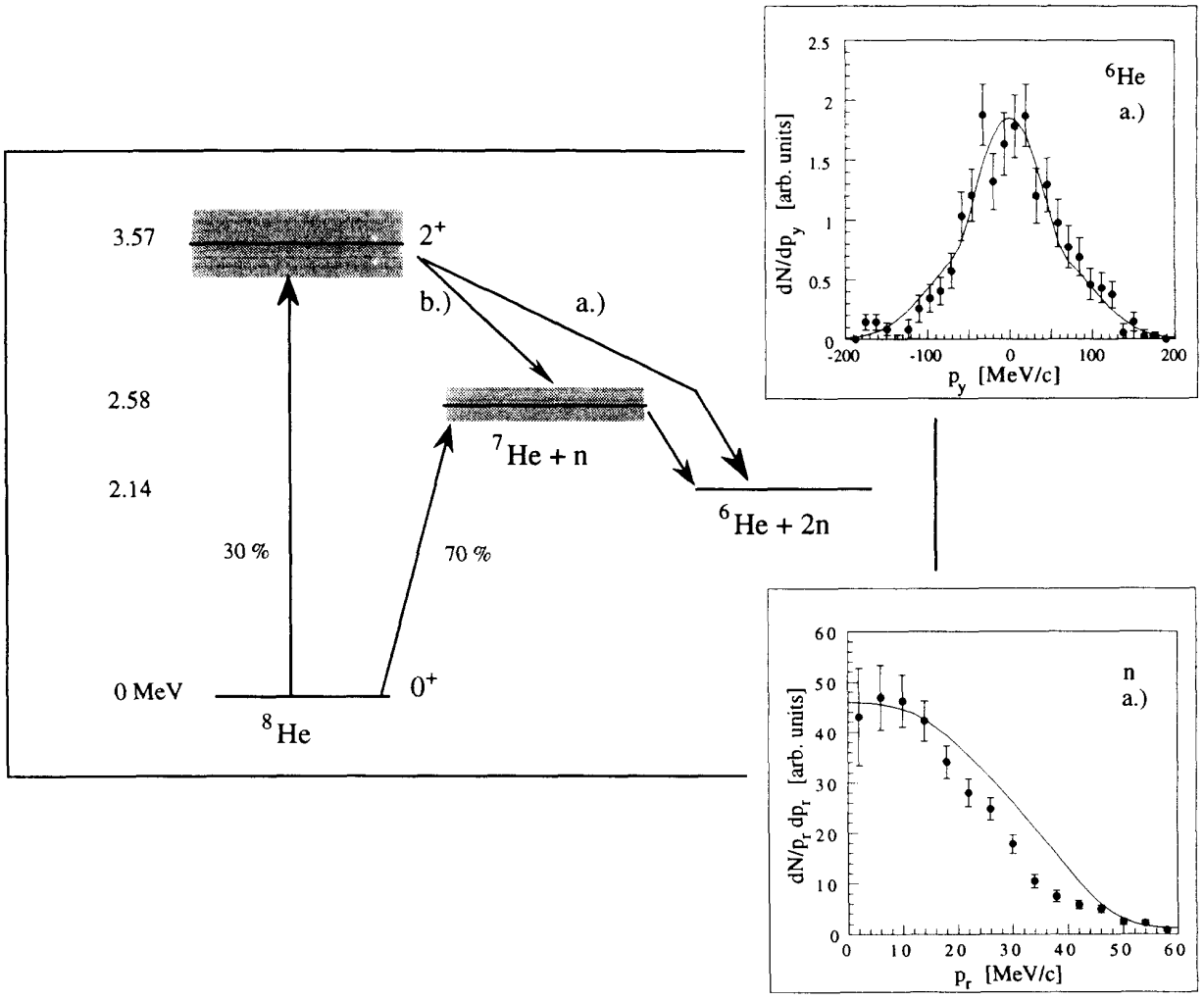

Figure 9: Sequential decay mechanisms for ^{8}He fragmentation. The ^{8}He* (J^π=2$^+$) state (E=3.57 MeV, Γ=0.5 MeV) lies above the ^{6}He+2n and ^{7}He+n threshold and will therefore decay, a.) directly or b.) sequential via the ^{7}He resonance, into a ^{6}He fragment and two neutrons. Both calculations give essentially the same result for the ^{6}He and neutron momentum distributions. The upper inset shows the ^{6}He transverse momentum distribution calculated with a 30% admixture of the decay a.) via the ^{8}He*, resonance. The lower inset shows the corresponding radial neutron momentum distribution. The experimental data are the same as in figure 6 and 7.

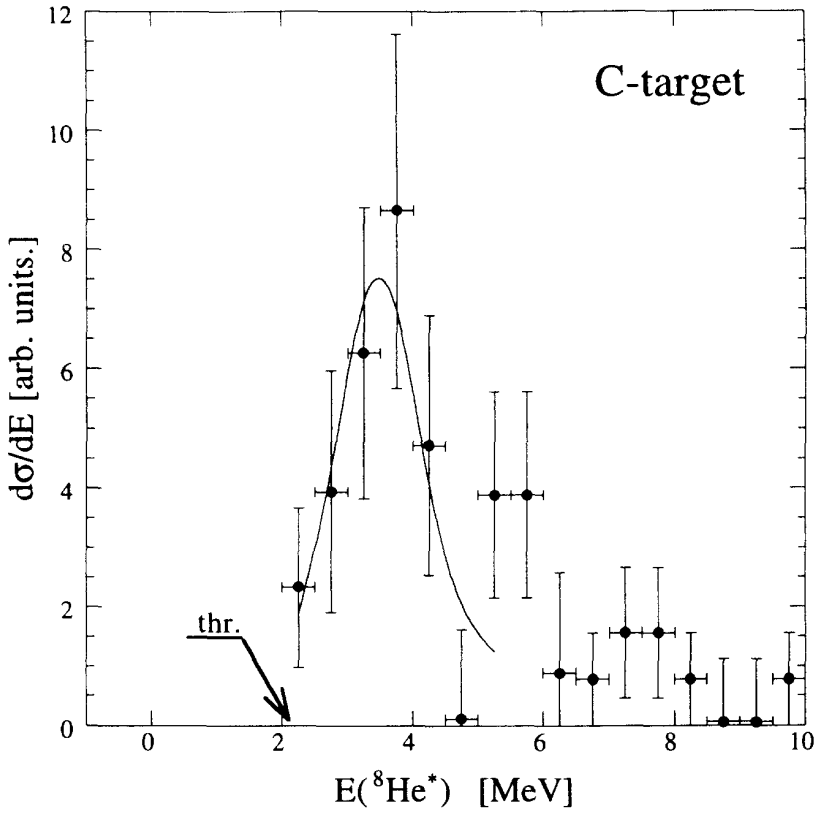

Figure 10: The ^{8}He* excitation energy spectrum deduced from the invariant mass of the ^{6}He+n+n channel from dissociation of ^{8}He at 240 MeV/u. The arrov indicates the ^{6}He+2n threshold at 2.14 MeV.

From these studies we may conclude that additional experimental data for different ^{8}He projectile energies as well as further theoretical investigations are needed to understand the reaction mechanisms and the detailed structure for the very neutron-rich nucleus ^{8}He. Very essential information could be obtained from studies of the $^8\text{He} \rightarrow \alpha + 4\text{n}$ channel at different energies and on different targets.

6 Acknowledgements

The authors are indebted to J. Kolata for providing results prior to publication and J.S. Vaagen for discussions and suggestions.

This work was supported by the German Federal Minister for Research and Technology (BMFT) under Contracts 06 DA 665 I, 06 BO 103, 06 OF 112 and 06 MZ 106 and by GSI via Hochschulzusammenarbeitsvereinbarungen under Contracts DARIK, OF ELZ, MZ KRD and partly supported by the Polish Committee of Scientific Research under Contract PB1158/P3/92/02, EC under contract ERBCHGE-CT92-0003 and CICYT under contract AEN92-0788-C02-02 (MJGB).

References

[1] A.C. Mueller and B.M. Sherrill, Annu. Rev. Nucl. Part. Sci. **43** (1993) 529

[2] H. Geissel, G. Münzenberg and K. Riisager, to be published in Annu. Rev. Nucl. Part. Sci. (1995)

[3] I. Tanihata, H. Hamagaki, O. Hashimoto, Y. Shida, N. Yoshikawa, K. Sugimoto, O. Yamakawa, T. Kobayashi, N. Takahashi, Phys. Rev. Lett. **56** (1985) 2676.

[4] K. Riisager Rev. Mod. Phys. **66** (1994) 1105.

[5] P.G. Hansen, A.S. Jensen and B. Jonson, to be published in Annu. Rev. Nucl. Part. Sci. (1995).

[6] I. Tanihata, D. Hirata, T. Kobayashi, S. Shimoura, K. Sugimoto, H. Toki, Phys. Lett. **B289** (1992) 261.

[7] M.J.G. Borge, M. Epherre-Rey-Campagnolle, D. Guillemaud-Mueller, B. Jonson, M. Langevin, G. Nyman, C. Thibault, and the ISOLDE collaboration, Nucl. Phys. **A460** (1986) 373.

[8] M.J.G. Borge, L. Johannsen, B. Jonson, T. Nilsson, G. Nyman, K. Riisager, O. Tengblad, K. Wilhelmsen Rolander and the ISOLDE collaboration, Nucl. Phys. **A560** (1993) 664.

[9] T. Kobayashi, O. Yamakawa, K. Omata, K. Sugimoto, T. Shimoda, N. Takahashi and I. Tanihata, Phys. Rev. Lett. **60** (1988) 2599.

[10] H. Geissel, P. Ambruster, K.H. Behr, A. Brünle, K. Burkard, M. Chen, H. Fogler, B. Franczak, H. Keller, O. Klepper, B. Langenbeck, F. Nickel, E. Pfeng, M. Pfützner, E. Roeckl, K. Rykaczewski, I. Schall, D. Schardt, C. Scheidenberger, K.-H. Schmidt, A. Schröter, T. Schwab, K. Sümmerer, M. Weber, G. Münzenberg, T. Brohm, H.-G. Clerc, M. Fauerbach, J.-J. Gaimard, A. Grewe, E. Hanelt, B. Knödler, M. Steiner, B. Voss, J. Weckenmann, C. Ziegler, A. Magel, H. Wollnik, J.P. Dufor, Y. Fujita, D.J. Viera and B. Sherrill, Nucl. Instr. Methods **B70** (1992) 286.

[11] The ALADIN Collaboration, GSI Scientific Report, Darmstadt, (1989) 292.

[12] Th. Blaich, Th.W. Elze, H. Emling, H. Freiesleben, K. Grimm, W Henning, R. Holzmann, G Ickert, J.G. Keller, H. Klingler, W. Kneissl, R. König, R. Kulessa, J.V. Kratz, D. Lambrecht, J.S. Lange, Y. Leifels, E. Lubkiewicz, M. Proft, W. Prokopowicz, C. Schütter, R. Schmidt, H. Spies, K. Stelzer, J. Stroth, W. Walus, E. Wajda, H.J. Wollersheim, M. Zinser and E. Zude, Nucl. Instr. Meth. **A314**, 136 (1992) and LAND Collaboration, GSI Scientific Report (1993).

[13] M. Zinser, Doktorarbeit Universit Mainz

[14] R.S. Henderson, O. Hausser, K. Hicks, C. Gunter, W. Faszer, R. Sawafta and N. Poppe, Nucl. Instr. Meth. **A254** (1987) 61.

[15] H. Simon, Diplomarbeit "Untersuchung an einem Magnetspektrometer für Experimente mit exotischen Strahlen", Technische Hochschule Darmstadt (1994), unpublished.

[16] F. Humbert, T. Nilsson, W. Schwab, M. Zinser, Th. Blaich, M.J.G. Borge, L.V. Chulkov, H. Eickhoff, Th.W. Elze, H. Emling, H. Freiesleben, H. Geissel, K. Grimm, D. Guillemaud-Mueller, P.G. Hansen, R. Holzmann, H. Irnich, B. Jonson, J.G. Keller, H. Klingler, J.V. Kratz, R. Kulessa, D. Lambrecht, Y. Leifels, A. Magel, M. Mohar, A.C. Mueller, G. Münzenberg, F. Nickel, G. Nyman, A. Richter, K. Riisager, C. Scheidenberger, G. Schrieder, B.M. Sherrill, H. Simon, K. Stelzer, J. Stroth, O. Tengblad, W. Trautmann, E. Wajda and E. Zude, Phys. Lett **B347** (1995) 198.

[17] T. Kobayashi, Proc. III RNB conf., MSU, (1993) 169

[18] F. Barranco, E. Vigezzi and R.A. Broglia, Phys Lett **B319** (1993) 387.

[19] M. Zinser, F. Humbert, T. Nilsson, W. Schwab, Th. Blaich, M.J.G. Borge, L.V. Chulkov, Th.W. Elze, H. Emling, H. Freiesleben, H. Geissel, K. Grimm, D. Guillemaud-Mueller, P.G. Hansen, R. Holzmann, H. Irnich, B. Jonson, J.G. Keller, H. Klingler, J.V. Kratz, R. Kulessa, D. Lambrecht, Y. Leifels, A. Magel, M. Mohar, A.C. Mueller, G. Münzenberg, F. Nickel, G. Nyman, A. Richter, K. Riisager, C. Scheidenberger, G. Schrieder, B.M. Sherrill, H. Simon, K. Stelzer, J. Stroth, O. Tengblad, W. Trautmann, E. Wajda and E. Zude, submitted to Phys. Rev Lett.

[20] A.A. Korsheninnikov and T. Kobayashi, Nucl. Phys. **A567** (1994) 97.

[21] M.V. Zhukov, B.V. Danilin, D.V. Fedorov, J.M. Bang, I.J. Thompson and J.S. Vaagen, Physics Reports **231** (1993) 151.

[22] A.A. Korsheninnikov M.V. Zhukov, M.H. Smedberg and T. Kobayashi, Europhys. Lett., **29** (1995) 359.

[23] M.V. Zhukov, A.A. Korsheninnikov and M.H. Smedberg, Phys. Rev **C50** (1994) R1.

[24] I. Tanihata, T. Kobayashi, O. Yamakawa, S. Shimoura, K. Ekuni, K. Sugimoto, N. Takahashi, T. Shimoda, H. Sato, Phys. Lett. **B206** (1988) 592.

[25] F. Ajzenberg-Selove, Nucl. Phys. **A490** (1988) 51.

[26] K. Riisager, Dr. scient thesis "Residence in forbidden regions", Aarhus University (1994), unpublished.

[27] K. Varga, Y. Suzuki, Y. Ohbayasi, Phys. ReV. **C50** (1994) 189.

[28] J. Kolata, private communication, 1995.

[29] K. Riisager, R. Anne, S.E. Arnell, R. Bimbot, H. Emling, D. Guillemaud-Mueller, P.G. Hansen, L. Johannsen, B. Jonson, A. Latimier, M. Lewitowicz, S. Mattsson, A.C. Mueller, R. Neugart, G. Nyman, F. Pougheon, A. Richter, M.G. Saint-Laurent, G. Schrieder, O. Sorlin and K. Wilhelmsen, Nucl. Phys **A540** (1992) 365.

[30] M.V. Zhukov and B. Jonson, Nucl. Phys. **589A** (1995) 1.

[31] M.V. Zhukov, L.V. Chulkov, D.V. Fedorov, B.V. Danilin, J.M. Bang, J.S. Vaagen, I.J. Thompson J. Phys. **G20** (1994) 201.

[32] A.A. Korsheninnikov, K. Yoshida, D.V. Aleksandrov, N. Aoi, Y. Doki, N. Inabe, M. Fujimaki, T. Kobayashi, H. Kumagai, C.-B. Moon, E.Yu. Nikolskii, M.M. Obuti, A.A. Ogloblin, A. Ozawa, S. Shimoura, T. Suzuki, I. Tanihata, Y. Watanabe and M. Yanokura, Phys. Lett. **B316** (1993) 38.